Remote Sensing of Environment 213 (2018) 61–72

Contents lists available at ScienceDirect

Remote Sensing of Environment

journal homepage: www.elsevier.com/locate/rse

Globally scalable alpine snow metrics

Nicholas E. Wayand[a,b,*], Christopher B. Marsh[a,b], Joseph M. Shea[a,c], John W. Pomeroy[a,b]

[a] Centre for Hydrology, University of Saskatchewan, Canada
[b] Global Institute for Water Security, University of Saskatchewan, Canada
[c] Geography Program, University of Northern British Columbia, Canada

ARTICLE INFO

Keywords:
Snowcovered area
Blowing snow
Avalanches
Snow ablation
Landsat 8
Sentinel 2
Google earth engine

ABSTRACT

Horizontal and altitudinal redistribution of snow by wind transport and avalanches can be important controls on small- and large-scale snow accumulation patterns that control meltwater supply in alpine environments. Redistribution processes control the spatial variability of snow accumulation, which not only controls meltwater supply, but also regulates snowmelt timing, duration, and rates, as well as snow-covered area depletion and the variable contributing area for meltwater runoff generation. However, most hydrological models and land surface schemes do not consider snow redistribution processes, and those that do are difficult to verify without spatially distributed snow depth measurements. These are rarely available in both high resolution and covering large scales. As an increased number of hydrological models include snow redistribution processes there is a need for additional snowcover metrics to verify snow redistribution schemes over large areas using readily available data.

This study develops novel high-resolution (20 m), snowcover indices from remotely sensed imagery (Landsat-8 and Sentinel-2) to evaluate snow redistribution models over alpine areas without in-situ or airborne snow observations. A snowcover absence (SA) index, calculated from snow-free areas during the winter, identifies areas of wind erosion or avalanche source areas. A snowcover persistence (SP) index, calculated from snow-covered areas during the summer, identifies snow deposition in drifts and avalanche deposits.

The snowcover indices captured the relative differences in surface observations of snow presence and absence between exposed and sheltered sites on an intensely instrumented ridge in the Canadian Rockies Hydrological Observatory. Within the Tuolumne River Basin in central California (1100 km^2), the SP index captured roughly half of the spatial variability (R^2 = 0.49 to 0.56) in peak SWE as estimated from airborne LiDAR-derived snow depths. At the individual mountain ridge scale (~800 m), variability in both ablation and snow redistribution controlled the SP patterns over 7979 ridges. Differences in shortwave irradiance explained 76% of the SP variance across ridges, but could not explain smaller-scale (~100 m) SP peaks that are associated with snowdrifts and avalanche deposits. The snowcover indices can be used to evaluate snow redistribution models of the finer scale impacts of snow redistribution by wind and gravity as long as the larger scale influences of spatially variable solar irradiance effects are also simulated.

1. Introduction

Mountain snow is a critical natural reservoir of water resources for the world (Li et al., 2017; Meehl et al., 2007) and has significant economic impacts (Sturm et al., 2017). Over the Canadian Rockies, alpine terrain above treeline covers more than half of the total area and has a significant contribution to snowpack storage and the areal albedo. As blowing snow and avalanches dominate alpine snow redistribution, these processes must be represented in land surface models to accurately simulate surface energy and mass fluxes (Pomeroy et al., 1998). However, observations of horizontal snow transport are rare at the basin scale, posing a challenge for model development and evaluation.

Blowing snow observations fall into two categories: 1) direct measurements of snow saltation or suspension (Aksamit and Pomeroy, 2016; Bintanja et al., 2001; Brown and Pomeroy, 1989; Gubler, 1981; Schmidt and Jairell, 1987; Vionnet et al., 2017, 2013); and 2) indirect measurements of snow redistributions before and after blowing snow events (Fang and Pomeroy, 2009; MacDonald et al., 2010; Musselman et al., 2015; Pomeroy and Gray, 1995). Although direct measurements have been critical for understanding and developing the physics of blowing snow models, indirect methods are required to evaluate the impact of snow redistribution on snow hydrology over multiple scales (Palm et al., 2011). Indirect measurements include manual snow depth measurements across ridges (MacDonald et al., 2009), terrestrial LiDAR

* Corresponding author at: Department of Atmospheric Sciences, University of Washington, USA
E-mail address: nicway@uw.edu (N.E. Wayand).

https://doi.org/10.1016/j.rse.2018.05.012
Received 27 January 2018; Received in revised form 28 April 2018; Accepted 7 May 2018
Available online 12 May 2018
0034-4257/

(Grünewald et al., 2010; Prokop, 2008; Schirmer et al., 2011; Schön et al., 2015), and airborne LiDAR (Deems et al., 2006; Hopkinson and Chasmer, 2009). The use of operational airborne LiDAR has become more common and feasible over many basins (Painter et al., 2016), however, it still remains expensive when deployed on airplanes or drones and so is often limited to specialized field campaigns.

As an alternative to terrestrial based approaches, satellite based remote sensing can provide global coverage with varying temporal and spatial resolutions. In alpine terrain, Bernhardt et al. (2010) used 30 m snowcover from two Landsat images to evaluate a distributed blowing snow model, finding the model's spring snowcover was too homogenous compared with observations. Macander et al. (2015) utilized 11,645 Landsat scenes over Alaska to develop climatological snow disappearance maps to characterize caribou habitat, but stopped short of identifying snow redistribution. Déry et al. (2005) used daily fractional snowcover from the Moderate Resolution Imaging Spectroradiometer (MODIS) to inform snowcover depletion curves within a land surface model in order to capture persistent snowdrifts in the Arctic. Blowing snow events have also been identified over the gentle terrain of Antarctica (Scarchilli et al., 2010) using satellite based LiDAR and MODIS. Over complex terrain, the MODIS snowcover products at a nominal 500 m resolution are too coarse to resolve snowdrifts caused by blowing snow. Snow redistribution features such as snowdrifts normally occur at scales from 1 mm to roughly 100 m (Aksamit and Pomeroy, 2016; Clark et al., 2011; Pomeroy and Gray, 1995).

The objectives of this study are to identify mountain regions dominated by snow redistribution, and develop snowcover indices suitable for testing snow redistribution models over large spatial domains ($> 1000\ km^2$). The approach takes advantage of multi-year and multi-platform snowcover records by focusing on Landsat-8 and Sentinel-2A imagery, at 30 m and 20 m resolutions, respectively that can resolve many snowdrift patterns. These platforms are limited by repeat times (16 days and 10 days, respectively) and cloud cover, but, combined, greatly increase the chances of capturing cloud-free temporal variations in snowcover patterns caused by blowing snow and avalanches.

The study domains and data used are described in Section 2. Section 3 details the derivation of snowcover indices and spatial analysis methods applied. Results of the evaluation of the indices and their pattern classification are provided in Section 4. A discussion of the applications and limitations of snowcover indices is given in Section 5 and summary conclusions in Section 6.

2. Study domains and data

2.1. Study domains and site measurements

Three study domains (Fig. 1a, e) are used for the analysis and evaluation of derived snowcover indices. The Fortress Mountain Snow Laboratory (hereafter Fortress) is located in the Canadian Rockies at 50.82°N, −115.21°W and ranges in elevation from 2100 m to 2890 m (red area in Fig. 1e, expanded in Fig. 1b). Fortress is part of the Canadian Rockies Hydrological Observatory and includes in-situ meteorological and snow measurements of an alpine environment representative of much of the eastern slopes of the Canadian Rockies. Data was collected between 2014 and 2018 (and continuing), thus overlapping temporally with remote observations (see Section 2.2). Two meteorological stations used for this study are shown in Fig. 1c. The exposed Fortress Ridgetop station (hereafter Exposed) is in a wind-exposed environment with frequent blowing snow erosion. In contrast, the sheltered Fortress Southface station (hereafter Sheltered) is located 70 m southeast of the ridge within a cluster small trees on a south facing slope. Sub-nival krummholz vegetation (Jones et al., 2001) results in the frequent deposition of windblown snow and locally deep snow accumulations. At both sites, snow depths were measured with ultrasonic sensors (SR-50) at 15-min intervals, and bi-weekly snow surveys near both sites measured snow depth and snow water equivalent (SWE) using an ESC-30 or Mount Rose sampler and scale following Pomeroy and Gray (1995). Incoming shortwave was measured at a 15-min sampling interval at the Exposed site with a Kipp & Zonen CNR4 net radiometer.

Areal evaluation of snowcover indices was conducted in the Tuolumne River Basin (black square in Fig. 1a, expanded in Fig. 1d) located in the central Sierra Nevada at 37.93°N, −119.57°W, because of the availability of multiple years of Airborne Snow Observatory (ASO) flight data (Painter et al., 2016). Painter et al. (2016) estimated SWE derived from LiDAR snow depth and Snobal density modeling, aggregated to a 50 m resolution. Data for the flights nearest to the timing of peak SWE were obtained. Quality controlled and gap-filled shortwave irradiance observations from the Tuolumne Meadows station (Lundquist et al., 2016) were used to drive calculations of spatially distributed shortwave irradiance across the domain following Dozier and Frew (1990).

The third study domain (white area in Fig. 1a, e) encompasses a west-east transect (hereafter Transect) across the Canadian Rockies (51.27 to 50.74°N and −119.13 to −113.91°W) to identify regional patterns in snow redistribution from the maritime to alpine to prairie snow climates (Sturm et al., 1995).

2.2. Satellite data

Landsat-8 and Sentinel-2A imagery were obtained and analyzed using the Google Earth Engine (GEE; Gorelick et al., 2017). The GEE workflow employed consisted of data import, cloud masking, shadow masking, forest cover masking, and normalized difference snow index (NDSI) (Hall et al., 1995) calculation and classification. The GEE code can be scaled globally.

For each study domain, Landsat-8 tiles and 16 Sentinel-2A tiles (Table 1) were obtained that contained < 30% cloud cover during each satellite's operational period (March 2013 to May 2017, and June 2015 to May 2017, respectively). The availability of pixels of varied seasonally (Fig. 2), due to higher cloud cover and shadowing during winter months. Landsat-8 clouds were masked using the GEE *simpleCloudScore* algorithm with a confidence value of 80%. This value was selected to provide the best classification of clouds over our study domains, but may not be optimal over other regions. Sentinel-2A clouds were masked using an algorithm similar to *simpleCloudScore* (*sentinelCloudScore*), after the quality control flags provided by the European Space Agency were found to perform unsatisfactorily over our study domains. The tile-average solar azimuth and solar zenith angles were used in conjunction with the Temporal Dark Outlier Method (Housman et al., 2015) to calculate cloud shadows for both satellites. Terrain shadow masking was especially important during winter months when large shadow areas occurred during overpasses. Terrain shadows were calculated using the GEE *hillshadow* algorithm and the 30 m resolution Shuttle Radar Topography Mission (SRTM) Version 3 void-filled DEM (Farr et al., 2007). Because SRTM only covers 56°S to 60°N, the ASTER GDEM product at 100 m spatial resolution can be used as an alternative but with less accurate shadow estimation (not used here). Forested areas were masked using the Hansen et al. (2013) tree cover dataset based on Landsat data; all 30-m pixels with tree cover > 30% were excluded from our analysis. Lakes were masked using the Pekel et al. (2016) dataset, where pixels with 70% annual water occurrence are discarded. Finally, the NDSI was used to classify snow pixels with NDSI values > 0.4 and non-snow pixels with NDSI values less than or equal to 0.4. Datasets were combined by resampling the Landsat-8 (30 m) to match the Sentinel-2A (20 m) grid, using the nearest neighbor approach.

2.3. Global environmental multiscale model shortwave irradiance

Observations of incoming shortwave irradiance are sparse over the

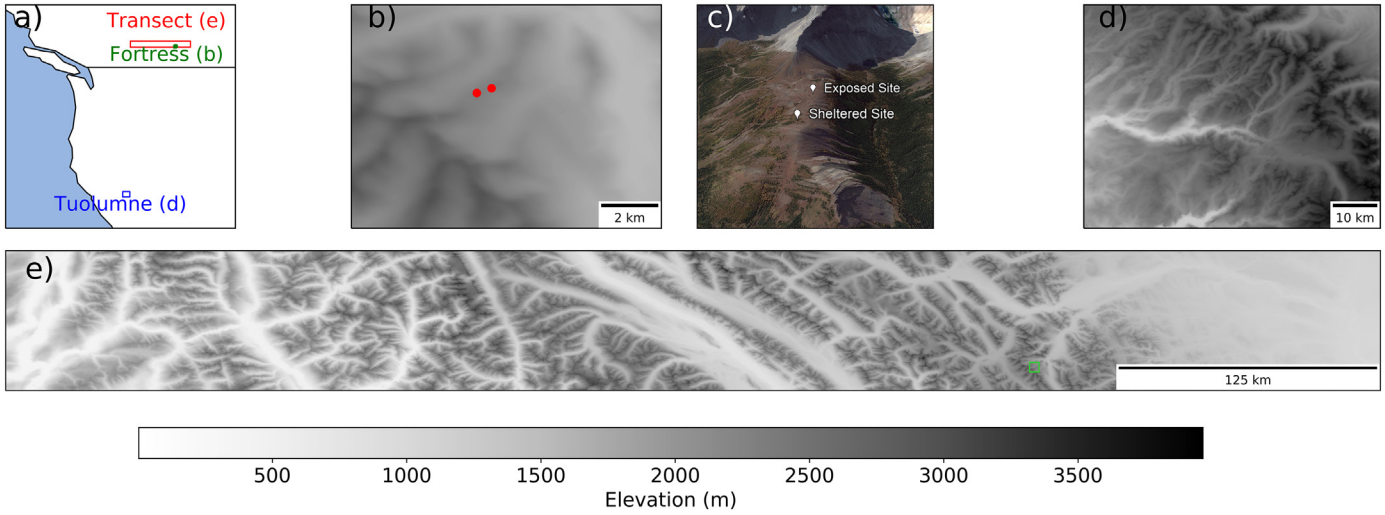

Fig. 1. (a) Map of study domain locations. (b) Fortress domain located in Canadian Rockies. (c) Perspective view looking south-west over Fortress Ridge. (d) Tuolumne River Basin located in southern Sierra Nevada. e) Transect across Canadian Rockies used for regional indices analysis.

Table 1
Number of Landsat-8, Sentinel-2A tiles available and used for calculating the SP and SA, for each domain.

Domain	Landsat-8 tiles < 30% cloud	Sentinel-2A tiles < 30% cloud	SP tiles (April–August)	SA tiles (November–March)
Fortress	77	18	61	34
Transect	300	56	220	136
Tuolumne	264	214	309	169

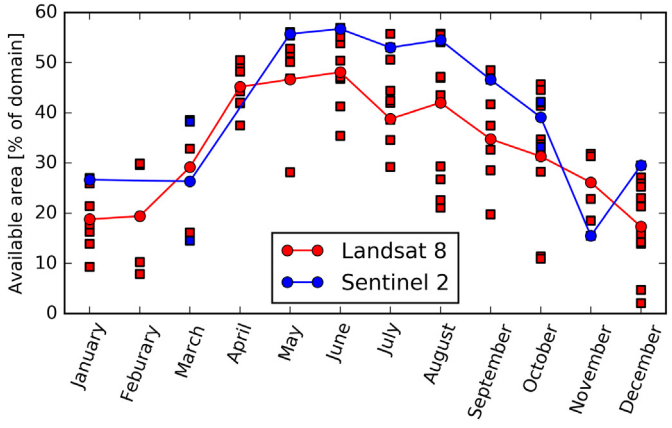

Fig. 2. Availability of pixels classified as snow or soil from Landsat 8 (red) and Sentinel 2 (blue) over the Fortress study domain. Forest coverage is 41%. Squares show coverage of individual tiles for all years of a given month. Circles with lines show monthly means for all available years (2013–2017). (For interpretation of the references to colour in this figure legend, the reader is referred to the web version of this article.)

Transect domain, and so output from Environment and Climate Change Canada's Global Environmental Multiscale Model (GEM) at 2.5 km resolution was assessed. The 00Z 48-h forecasts were archived between November 2014 and August 2016, and combined into a continuous time series by selecting only the 6 to 30 forecast hours. GEM shortwave irradiance values were then downscaled to account for slope and shading of terrain below the 2.5 km resolution, as described in Section 3.2.1.

3. Methods

3.1. Snowcover indices development and evaluation

3.1.1. Snowcover indices

To capture spatial patterns of snow deposition and erosion, Snow Persistence (SP) and Snow Absence (SA) indices are proposed. SP represents the normalized snowcover duration between April and August and is calculated for each pixel as:

$$P = \frac{N_{snow}}{N_{total}} \quad (1)$$

where N_{snow} is the total number of snow covered days (Fig. 3a) and N_{total} is the total number of images available (Fig. 3c). Resulting SP values (Fig. 3e) ranged from 0 (always snow free) to 1 (always snowcovered). Because N_{total} was not the same for all pixels due to satellite footprints and the presence of cloud and shadows, pixels where N_{total} was < 20% of the domain maximum N_{total} were masked to remove poorly sampled data points from the analysis. This step primarily removed pixels on steep north-facing slopes that were subject to shadowing, which represented 0.9% of the Fortress domain, 0.3% of the Transect domain, and 0.9% of the Tuolumne domain by area.

The SP index methodology was repeated to calculate SA (Fig. 3b,d,f), using images taken between November and March when continuous snowcover is expected. The SA is calculated as:

$$SA = \frac{N_{bare}}{N_{total}} \quad (2)$$

where N_{bare} is the total number of snow-free days at each pixel. SA values ranged from 0 (always snowcovered) to 1 (always snow free). Over the Fortress domain, SA values were mostly 0 except for the ridge in the upper right of Fig. 3f. GEE scripts to produce snowcover indices are provided at (https://code.earthengine.google.com/0fc31697a8cd8a961b7c4a1929c8c5a0).

3.1.2. Point evaluation: Fortress stations

At Fortress, calculated SP and SA values were compared to measured snow depths and snowcover durations at pixels covering the station towers and snow survey sites. Relative differences in snowcover for the Exposed and Sheltered sites on Fortress Ridge were examined through station data (Fig. 1c) and snow redistribution indices.

3.1.3. Distributed evaluation: Tuolumne ASO measurements

Snowcover indices calculated for Tuolumne (2013–2016) were

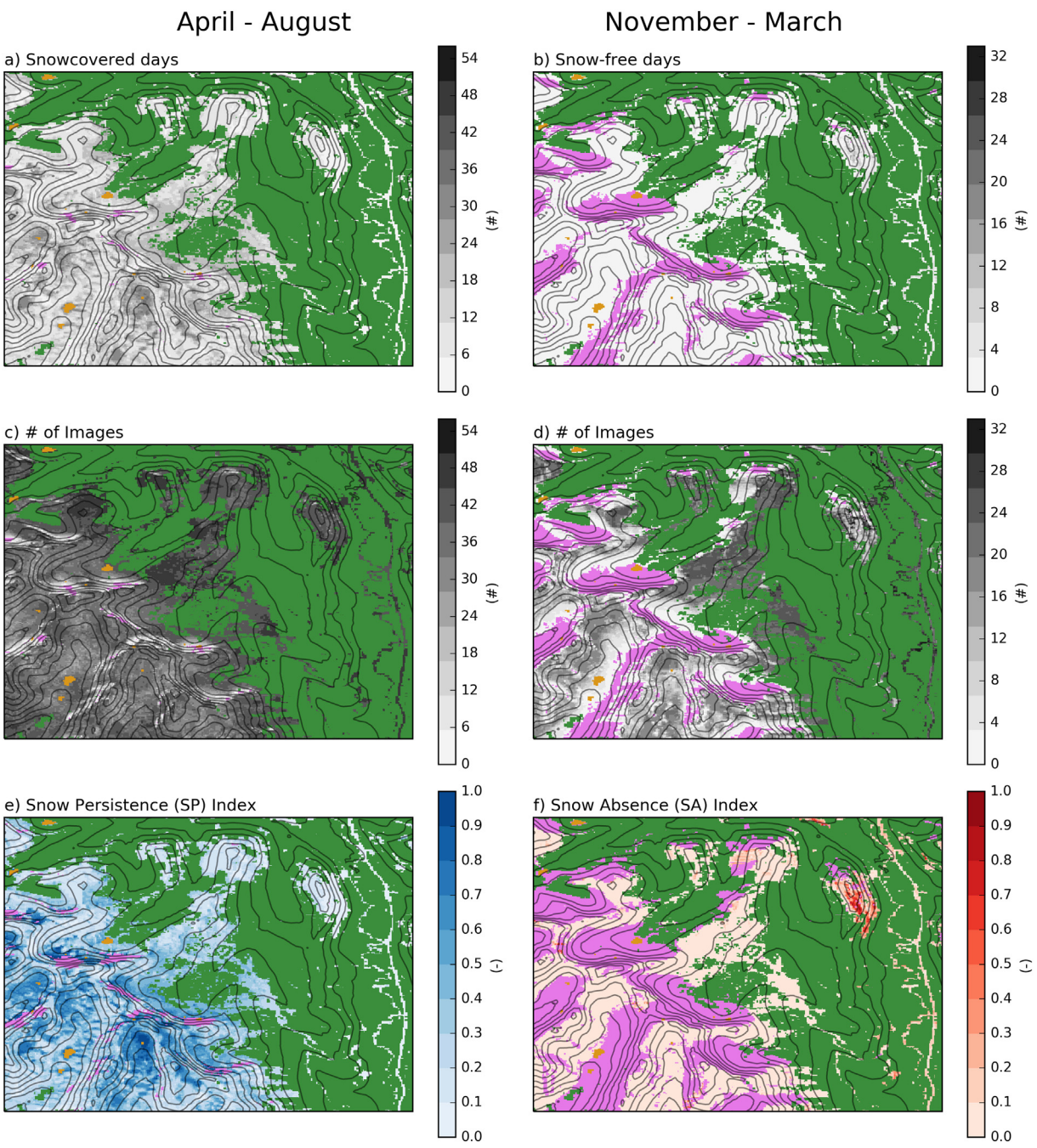

Fig. 3. Total number of snowcovered days between April and August (a) and snow-free days between November and March (b), at each pixel for years 2013 to 2017. (c, d) Total number of available (not cloud, not shadow, not missing) images at each pixel, for each month range. Note different colour bar limits between SA and SP. The normalized SP values (e) and SA values (f). *Dark green* pixels indicate forest, *orange* pixels water, and *magenta* pixels insufficient number of images available (i.e. due to shadowing). Linear features at right of domain are highway-40 and local service roads. *Black contours* show elevation increments of 100 m. (For interpretation of the references to colour in this figure legend, the reader is referred to the web version of this article.)

compared to LiDAR-based SWE over the Tuolumne domain by resampling SP indices (20 m resolution) to the 50 m SWE grid. For each water year (2013–2016), the ASO flight nearest to peak SWE was used to evaluate the snowcover indices' ability to capture SWE spatial variability.

3.2. Ablation vs. snow redistribution effects on snow persistence

Assuming that differences in snow duration between pixels was primarily due to snow accumulation and not ablation (snowmelt + sublimation) energy is fundamental to development of the SP index. To test the hypothesis that ablation energy controls the SP spatial pattern, SP values were compared against the primary source of ablation energy: shortwave irradiance. The comparison was made over the full extent of each study domain and over individual mountain ridges. Mountain ridges are of interest because they have both the largest spatial differences in shortwave irradiance as well as high rates of snow redistribution due to high winds and steep slopes.

3.2.1. Shortwave irradiance calculations

Distributed maps of incoming shortwave radiation were calculated over the Fortress and Tuolumne domains using in-situ observations and

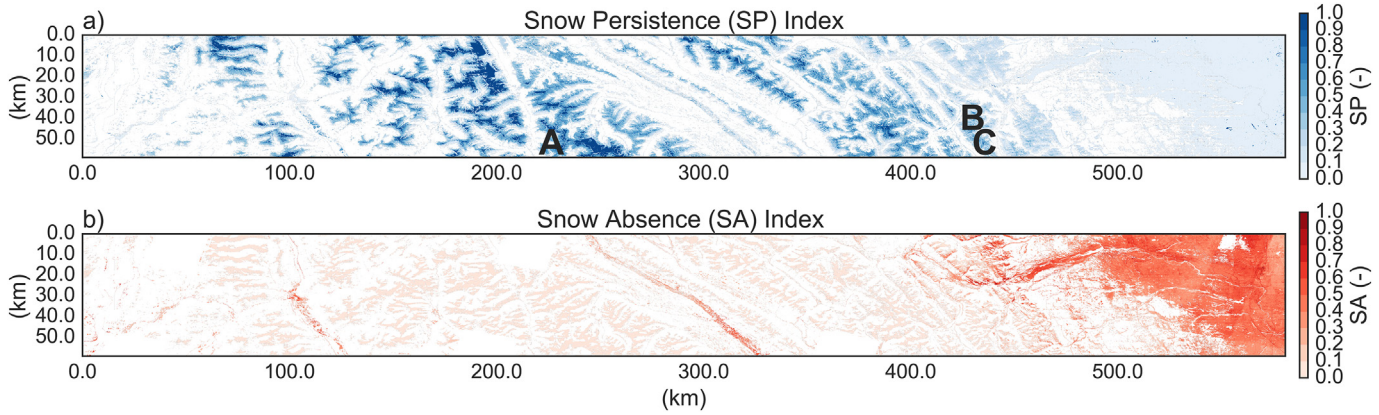

Fig. 4. SP (a) and SA (b) values using images from yeas 2013 through 2016 over the Canadian Rockies transect. Letters in (a) show locations referred to in Fig. 5.

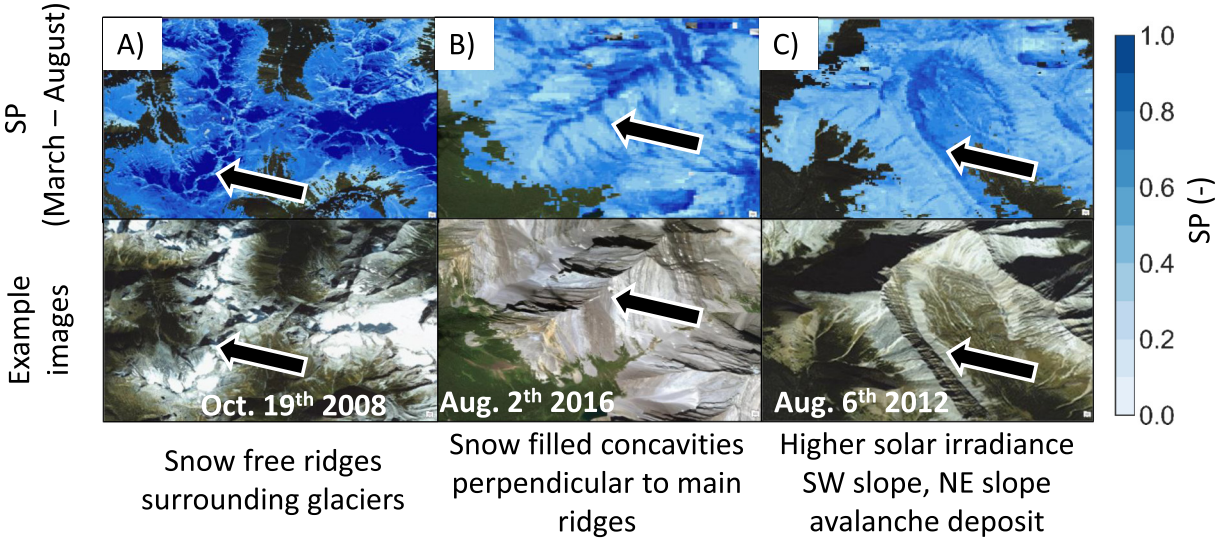

Fig. 5. Examples of reoccurring patterns of SP values within the transect domain and high-resolution imagery. Locations shown in Fig. 4a. Black arrows indicate discussed features. Note the example images are from different times than the SP index (March to August) to illustrate the terrain. Source: WorldView-3 DigitalGlobe.

over the Transect domain using GEM output. The Fortress Ridge station (Exposed) was selected for the Fortress domain, as it has minimal terrain shading and the radiometer dome remains snow-free due to persistent high wind speeds. Similarly, the Tuolumne station was selected because it has undergone careful quality control and in-filling following Lapo et al. (2015). Hourly GEM irradiance values at the 2.5 km grid were downscaled to the snowcover indices resolution (20 m) using the nearest neighbor approach. An evaluation of GEM shortwave with measurements at the Exposed station found a bias of $-35\ W\ m^{-2}$ and a coefficient of determination of 0.67.

Shortwave irradiance was then adjusted for each domain based on slope and aspect using Garnier and Ohmura (1970), and terrain shadows were calculated at hourly time steps following Dozier and Frew (1990). See (https://github.com/Chrismarsh/CHM) for code used. Finally, the accumulated shortwave irradiance ($MJ\ m^{-2}$) during SP months (April to August) of years 2014 through 2016 was calculated and compared to SP values over each domain.

3.2.2. Ridge identification and analysis: Fortress domain

Individual ridges were identified using the highest resolution terrain dataset available: the Canadian Digital Elevation Model (Natural Resources Canada, 2007) at a 0.75 arc *sec* (≈23 m) spatial resolution. First, the second eigenvalue of the Hessian matrix was calculated to isolate concave features. Then, Otsu (1979) global thresholding and Zhang and Suen (1988) skeletonization was applied to produce ridges with single pixel widths. Finally, the probabilistic Hough line detection (Hough, 1962) was used to identify individual linear ridges > 400 m in length, resulting in 38,716 ridges identified over the Transect domain.

Elevation, shortwave irradiance, and SP pixel values were extracted within a distance of 400 m perpendicular to each side of the linear ridge. A distance of 400 m was used to capture the majority of snowdrifts and avalanched deposits (MacDonald et al., 2010; De Scally, 1992). To identify persistent snow features parallel to ridges (see Section 4.1), the profiles along each ridge were averaged to derive 800 m profiles of elevation, shortwave irradiance, and SP. Ridges were excluded if they had elevation profiles that, 1) had a vertical elevation change of < 20 m (removed small ridges), 2) a maximum elevation away from the detected ridgeline (removed secondary overlapping ridges), or 3) had > 20% of missing SP values. This resulted in a subset of 7979 ridges.

A statistical association between profiles of shortwave irradiance to snow persistence and the maximum snowmelt due to differences in shortwave irradiance across the ridge was estimated using the coefficient of determination (R^2). An index of potential snowmelt was

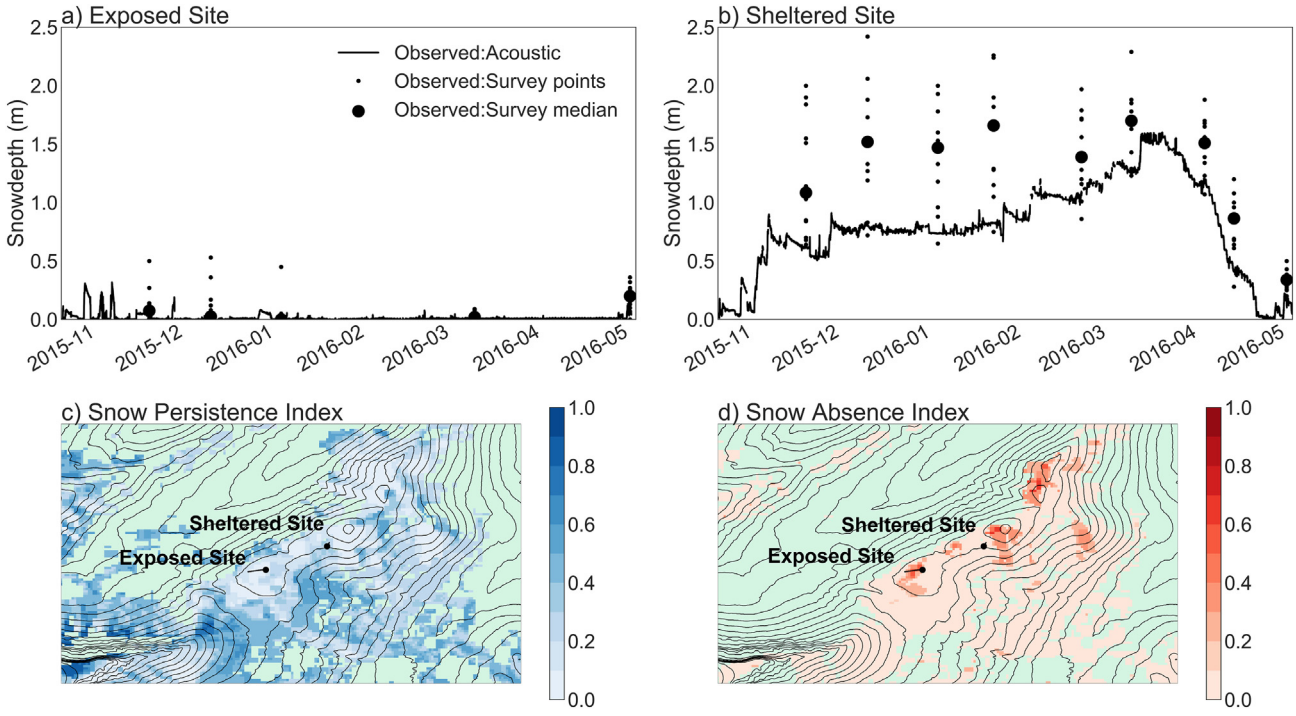

Fig. 6. Observed snow depths at the (a) Fortress Ridgetop (Exposed) and (b) Fortress Southface (Sheltered) stations (locations shown in Fig. 1c). Individual dots show all snow survey measurements, while large dots show median of each survey. Snow persistence index (c) and snow absence index (d) over Fortress Ridge, with locations of the Exposed site and Sheltered site (*black dots*) and survey transects (*black lines*). Note, the Sheltered transect is only 50 m long and not visible in plot. *Black contours* show elevation in 30 m increments. *Light green* pixels indicate either forest or insufficient number of images available due to cloud or shadow. Indices were calculated using Landsat-8 and Sentinel-2A images from November 2015 to August 2016. (For interpretation of the references to colour in this figure legend, the reader is referred to the web version of this article.)

calculated by assuming a) an average late spring/early summer albedo of 0.6, b) all energy goes into snowmelt, and c) snow lasts until August. It is a maximum estimate because violation of assumptions will lead to less snowmelt (e.g. the albedo is likely be higher, energy will also go into internal changes and turbulent heat fluxes, and snow will disappear before August). The maximum snowmelt difference across the ridge helps to interpret whether high correlations between shortwave irradiance and snow persistence are causative.

4. Results

4.1. Snow patterns across the Canadian Rockies Transect

SP values generally increased going east to west across the Transect domain (Fig. 4a) because of higher snow accumulations to the west. Regions with SP values of one indicate permanent snow or ice cover between the months of April and August. Over glaciers defined by the Randolph Glacier inventory (RGI Consortium, 2017), SP values averaged 0.97. Because SP values go to unity over glaciers, snow redistribution patterns cannot be identified on glaciers or permanent snowfields.

During the mid-winter months, SA values (Fig. 4b) remained at or near zero across the majority of the Rockies but started to increase along the eastern foothills and reach maximum values over the prairies. The increase in snow-free areas during mid-winter months along the eastern foothills may be caused by a combination of lower snow accumulations due to scouring by wind transport of snow and higher melt or sublimation from frequent chinook events (Golding, 1978; MacDonald et al., 2010; Pomeroy and Li, 2000; MacDonald et al., 2018).

An examination of SP spatial patterns in three representative areas revealed three reoccurring patterns (Fig. 5). Over the coldest regions and highest elevations, the ridges that surround glaciers were scoured free from snow (low values of SP on ridges, Fig. 5a). For the majority of non-glacial alpine areas, two patterns dominate: 1) high SP values in gullies perpendicular to main ridges (Fig. 5b, and 2) high SP values parallel and offset of the main ridge (Fig. 5c). Both features are influenced by a combination of variable patterns of ablation rates and of snow redistribution (blowing snow and avalanching) (Musselman et al., 2015; Pomeroy et al., 2004; De Scally, 1992). Therefore, these ridges are a challenging test for snow redistribution and ablation models, as they must accurately represent each process, and their interactions, to capture observed SP patterns. Controls on mountain ridge snowcover are further examined in Section 4.3.2.

4.2. Evaluation of Snowcover indices

4.2.1. Fortress in-situ snow observations

In-situ snowdepth measurements were used to evaluate how snowcover indices capture observed SP and SA patterns over Fortress Ridge. The dominant wind direction at the ridge stations during winter months is from the south-west, parallel to Fortress Ridge, which means that snow drifts form in topographical features or vegetation patches running perpendicular to the ridge. At the Exposed site (Fig. 6a), snow depths rarely exceeded 0.25 m before being wind-scoured, while at the Sheltered (Fig. 6b) site a maximum snow depth of 1.5 m occurred in the winter of 2015–2016. These observation agree with the remotely sensed SP index for the 2016 spring and summer (Fig. 6c), which is greater at the Sheltered site (SP = 0.25) than the Exposed site (SP = 0.07). During mid-winter months, the SA index (Fig. 6d) at the Exposed site (SA = 0.50) was greater than that observed at the Sheltered site (SA = 0.00), which qualitatively agrees with the time series of snow depth in Fig. 6b.

4.2.2. Tuolumne LiDAR peak SWE

LiDAR-based SWE estimates in the Tuolumne River Basin,

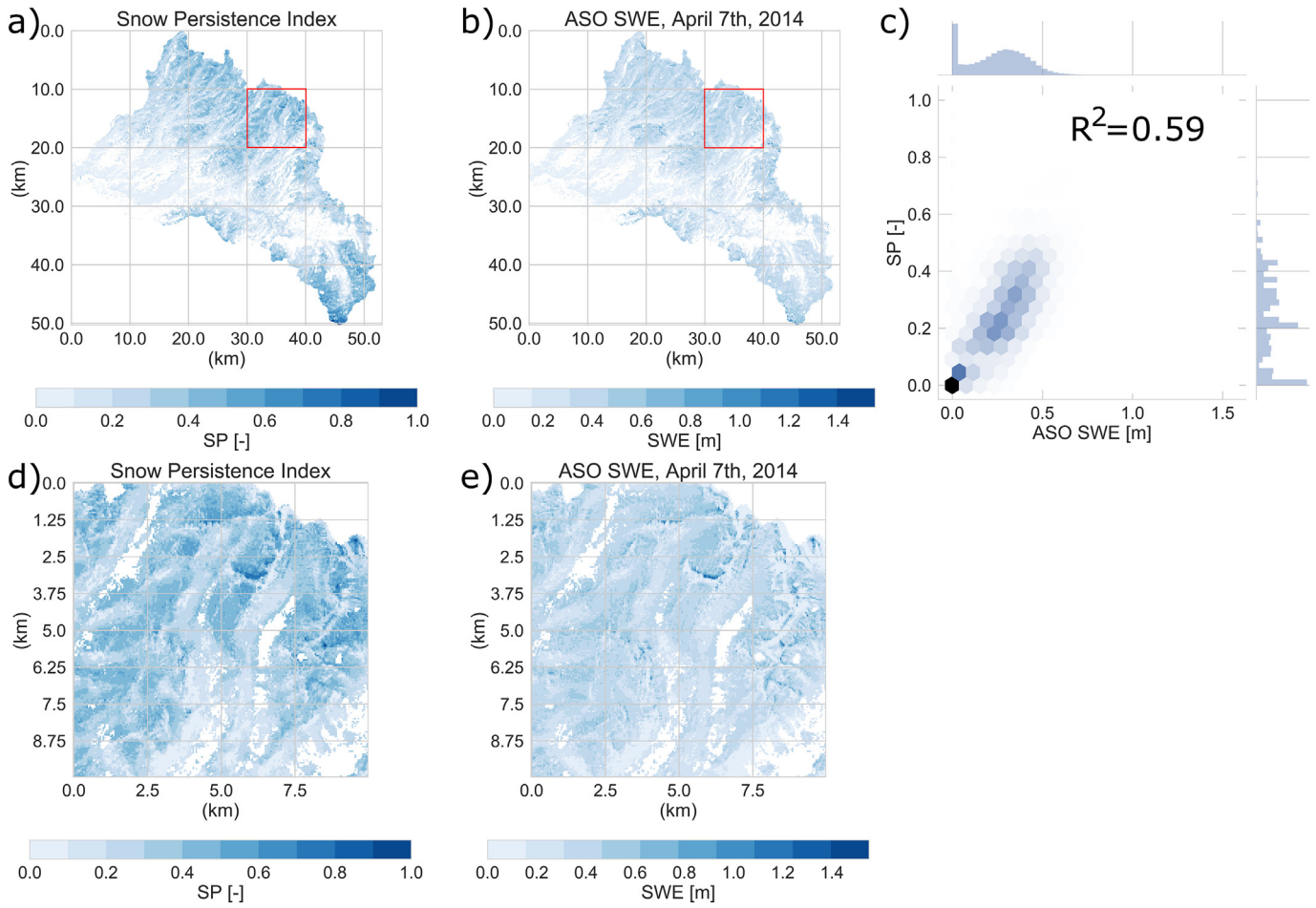

Fig. 7. Tuolumne River Basin (a) SP index for images between April and August 2014 and (b) ASO estimated SWE on April 7th, 2014. (c) Heatmap comparing (a) and (b). 1-D histograms on top and right of (c) show frequency of ASO SWE and SP values, respectively. Zoomed in views of the red outlines in (a) and (b) are shown in (d) and (e), respectively. (For interpretation of the references to colour in this figure legend, the reader is referred to the web version of this article.)

California, permitted evaluation of the role of snow redistribution in summer snow persistence. Fig. 7(a,b) illustrate estimated SP and peak SWE values for the 2013–2014 winter. SP values captured 59% of the spatial variability in peak SWE (Fig. 7c), which supports the hypothesis that snow persistence patterns are primarily controlled by the pattern of peak SWE accumulation. Fig. 7(d,e) show an enlargement of the region outlined in Fig. 7(a,b), which illustrates that SP values capture the locations of largest drift features in the lee of ridges (northeast). SP values captured 46% and 59% of the basin peak SWE variability during winters of 2014–2015 and 2015–2016, respectively (not shown). The reason for the lower correlation values during the 2014–2015 winter is not known, but may be due in part to record low snow accumulations associated with an anomalously warm and dry winter (Margulis et al., 2016).

4.3. Ablation vs. snow redistribution effects on snow persistence

4.3.1. Fortress and transect domain

The hypothesis that the pattern of spatially variable ablation energy controls snow persistence patterns was tested at all three domains. SP values showed no linear dependence with the shortwave irradiance within the Fortress domain (R^2 = 0.03, Fig. 8a), Transect domain

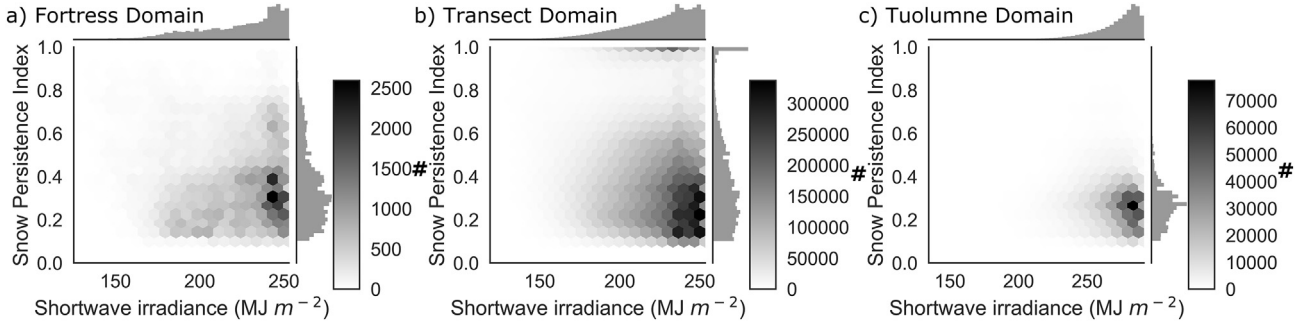

Fig. 8. 2-D histogram of snow persistence index versus the estimated accumulated shortwave irradiance values over the Fortress domain (a), Transect domain (b), and Tuolumne domain (c). 1-D histograms on top and right show frequencies of shortwave irradiance and snow persistence index, respectively. SP values < 0.1 were removed for clarity, which predominantly occurred over the prairies (see Fig. 4).

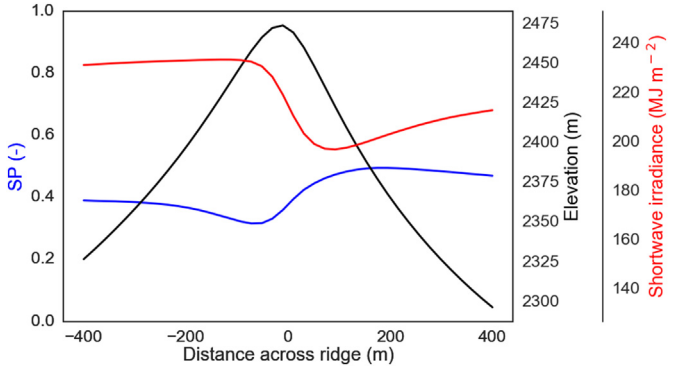

Fig. 9. Mean profiles of SP, elevation, and accumulated shortwave irradiance across all 7979 ridges within the transect domain. Ridges were oriented with the south facing slope to the left.

(R^2 = 0.09, Fig. 8b), or Tuolumne domain (R^2 = 0.04, Fig. 8c). These results suggest that differences in solar radiation (ablation) are not the primary control on SP patterns over these alpine regions. However, solar radiation may be locally important over mountain ridges, as examined below.

4.3.2. Mountain ridges

The average solar irradiance profile for all 7979 ridges in the Transect domain was highly negatively correlated (R^2 = 0.76) with the average SP profile (Fig. 9). This value is different from the entire domain correlations (R^2 = 0.03–0.09) because ridges cover roughly 40% of the Transect domain where shortwave irradiance variability is highest. The difference in average accumulated solar irradiance across ridges was 36 MJ m^{-2}, or an estimated 44 mm of equivalent snowmelt using assumptions in Section 3.2.2. Considering peak SWE values from nearby snowpillow stations average 681 mm, the 44 mm maximum snowmelt difference across ridges is relatively small. Therefore, although solar irradiance had high correlations across the majority of ridges, it is likely not the sole or primary cause of snow persistence patterns.

5. Discussion

5.1. Clustering ridge profiles

To elucidate the differences in snow persistence profiles across ridges, k-means clustering (Lloyd, 1982; Whitfield, 2017) was applied to all across-ridge SP profiles, normalized by their mean. Normalization removed regional differences in SP profiles but preserved variability across ridges. Five distinct cluster types emerged from this analysis (Fig. 10a) and correspond to the following SP profiles 1) *bare peak*, 2) *medium SP increase to the north*, 3) *large SP increase to the north*, 4) *no difference*, and 5) *increased SP to the south*. Fig. 10b–e illustrates an example ridge for each cluster type. *Bare peak* ridges (10.6% of all ridges) have equal snow persistence on either ridge face and predominately occur between glaciers or permanent snowfields. Because shortwave irradiance and orographic precipitation effects cannot explain the snow-free peaks, this suggests that blowing snow and/or avalanching redistributes this snow off the peak. The location of glaciers and snowfields below these peaks, which are known to be fed by

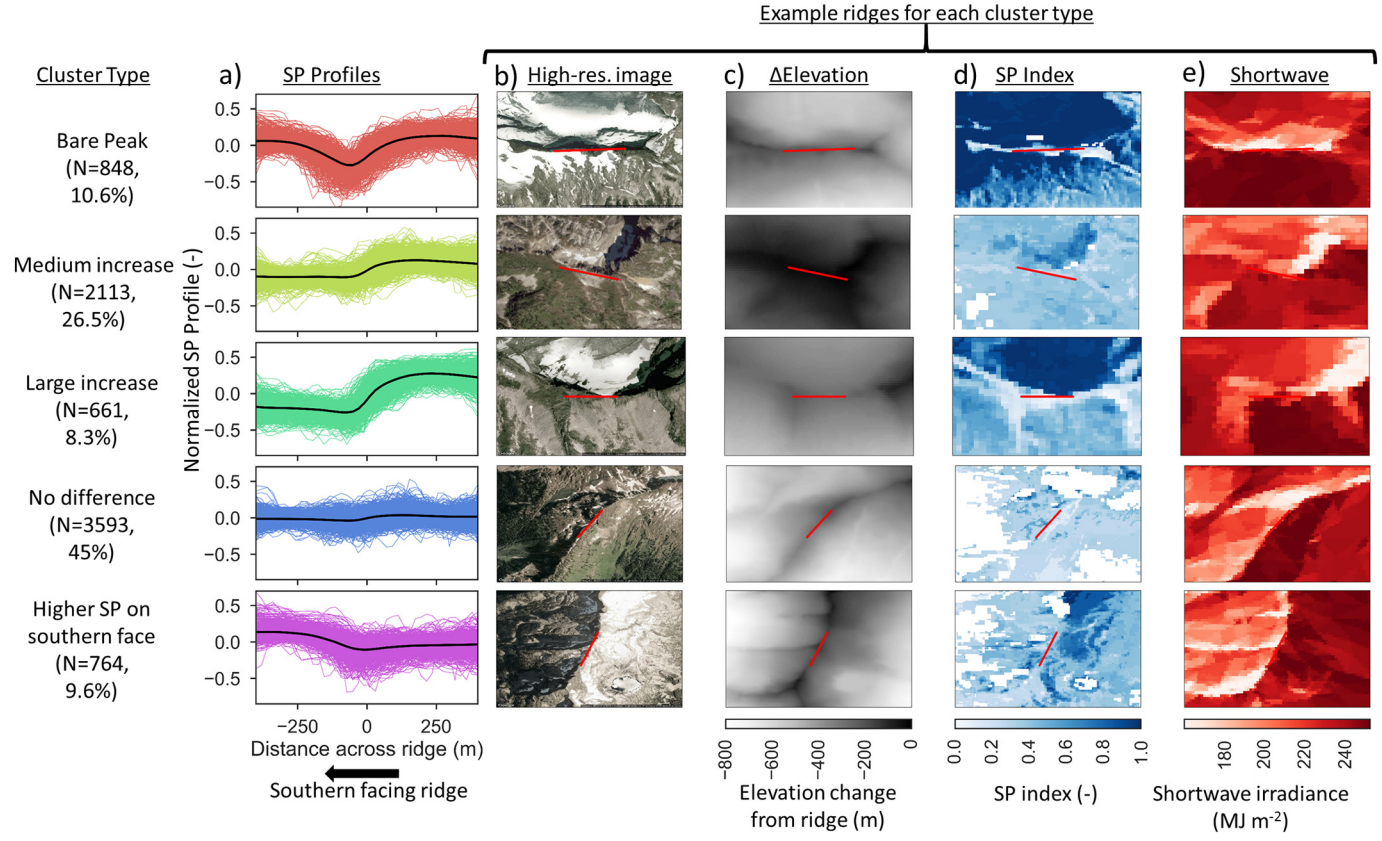

Fig. 10. Rows show the five clusters of ridges grouped by their SP profiles shown in (a). SP profiles in (a) are normalized by their mean to highlight the variance in SP across the ridge. Columns show example ridges for each cluster type, illustrating (b) high-resolution visible imagery, (c) change in elevation from ridge peak, (d) SP index, and (e) accumulated shortwave irradiance between March and August. *Black lines* in (a) show mean cluster SP profiles. *Red lines* in (b–e) show detected ridges. (For interpretation of the references to colour in this figure legend, the reader is referred to the web version of this article.)

wind-blown or avalanched snow, is consistent with this hypothesis (Benn and Evans, 1998; Dadic et al., 2010; Gascoin et al., 2013). *Medium and large increase to the north* cluster types (26.5% and 8.3%, respectively) represent a spectrum of ridges where snow persists on the north face. *No difference* clusters make up almost half (45%) of examined ridges and have no consistent pattern in SP across ridge profiles. Finally, the *increased SP to the south* cluster (9.6%) is interesting as snow persists longer on the southern facing side, contrasting the mean irradiance-SP relationship for all ridges (Fig. 9). An example of such a ridge is Fisera Ridge in Marmot Creek Research Basin where snow redistribution from north to south facing slopes causes persistence on the south face (DeBeer and Pomeroy, 2010; MacDonald et al., 2010; Musselman et al., 2015).

5.2. Snow drifts and avalanche deposits in SP profiles

SP profiles that are characterized by snow redistribution were identified within the individual ridge profiles. These signature SP profiles were defined as having a change in SP > 0.08 within a 120 m window (six 20 m pixels). Fig. 11a shows an example ridge where two local maxima in SP were detected (*black stars*). Ablation differences are likely not the driver of these persistent SP maxima, as the correlation coefficient (r) between SP and the solar irradiance within this window was −0.36 for the center peak and + 0.83 for the rightmost peak. The center peak is located on the south-facing slope 20 m from the ridgeline and is almost certainly a snowdrift. The rightmost peak is located 360 m from the ridge peak and at the bottom of a steep slope (max 54°), which likely indicates an avalanche deposit (Smith et al., 1994).

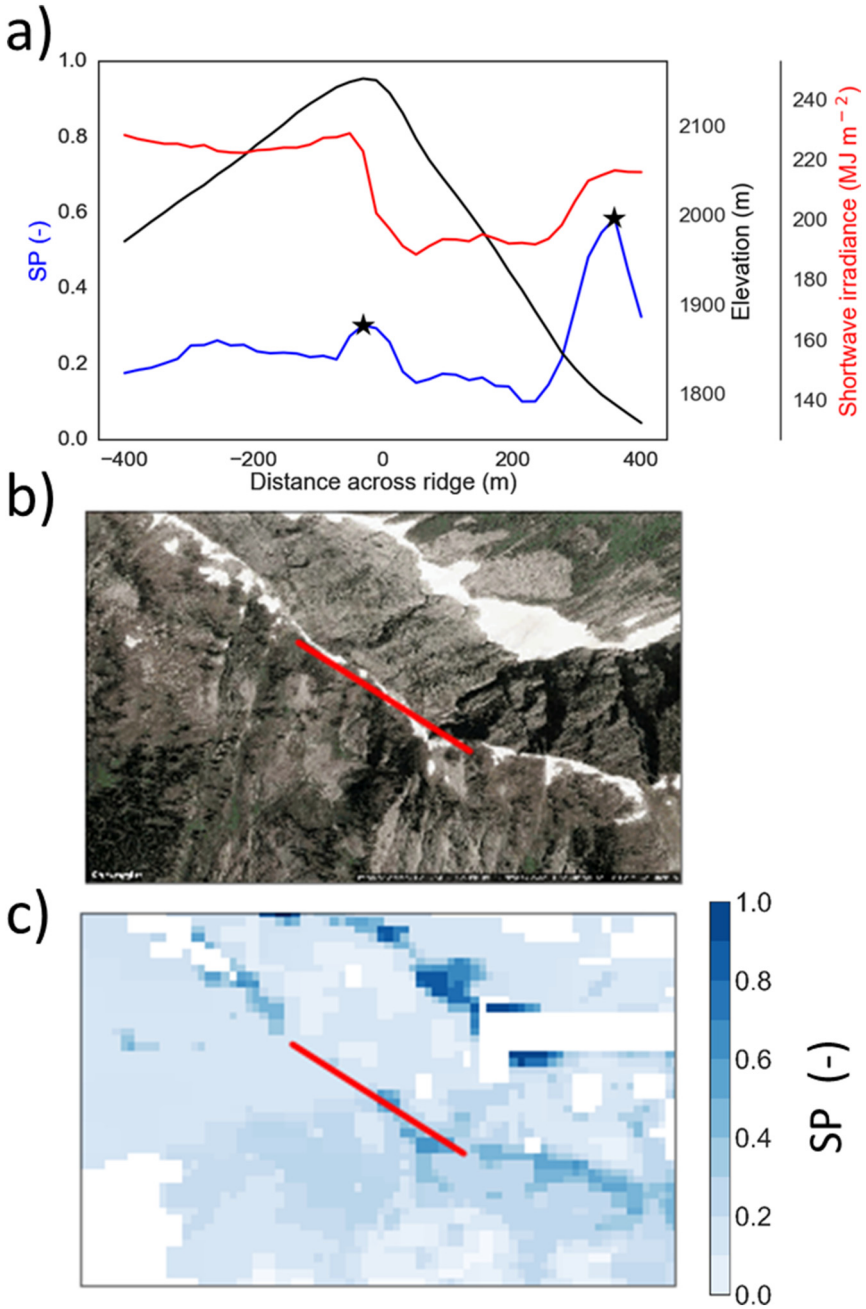

Fig. 11. Example ridge located in the Anstey Range in British Columbia (51.26344°, −118.706975°) with two identified SP maxima shown as *black stars* in the ridge profiles (a). High-resolution visible imagery shown in (b) and SP index in (c). *White* indicates missing SP values due to shadowing or vegetation coverage > 30%.

For all ridges where a SP maxima was identified ($N = 2219$), 264 (11%) had a SP/insolation correlation < -0.75, which suggests ablation is the primary control. For the remaining profiles ($N = 2065$), 89% had r values greater than -0.75, suggesting other processes than ablation may be important. Of these, 105 had SP maxima within 100 m of the ridgeline and had slopes $< 10^{\circ}$, and so were classified as likely snowdrifts. Avalanche deposits ($N = 1441$) were identified when SP maxima were located further than 100 m from the ridgeline and below a slope $> 20^{\circ}$. Identification of ridges where the primary control of snow persistence is snow redistribution make ideal test cases for snow redistribution schemes.

5.3. Limitations of snowcover indices

The snowcover indices presented here have a demonstrated utility and link to on-the-ground conditions. However, there are a number of limitations:

- SP values are always 1.0 over permanent snow or ice and therefore cannot capture avalanching or snow drifts for these areas. However, bare peaks surrounding glaciers (Fig. 11a) can be useful for evaluating redistribution schemes, where snow may be redistributed by wind and gravity to help feed glacier accumulation.
- Snowcover variability at scales less than the Sentinel-2A resolution of approximately 20 m could not be resolved, which means indices cannot capture narrow snowdrifts or narrow avalanche deposits. Note that the shortwave irradiance calculations are based on the highest resolution DEM (~23 m) that was widely available over the study domains. Thus, terrain features < 20 m that could have caused shadowing were missed by this model. However, shadows < 20 m would have caused persistent snowcover errors below the 20 m scale of remote sensing observations, and therefore should not affect these results.
- Sparse shrubs in alpine terrain will limit snow erosion and redistribution (Ménard et al., 2012) and may have influenced the SP patterns found here. The impact of shrubs on snow persistence indices could not be examined in the absence of a high-resolution alpine vegetation dataset.
- SA values during mid-winter months were missing on north facing slopes due to persistent shadowing at low solar altitudes. Future work should use a distinctive snow classification method for shadowed regions to expand the useable area of the SA index.
- The NDSI threshold value used here (0.4) worked well on average to classify snow but was not always optimal for a given image. A sensitivity test (not shown) found SP and SA *patterns* remained relatively unchanged while *absolute* values varied. SP values were most sensitive on north-facing slopes surrounding shadows. SA values were most sensitive on ridge lines and narrow gaps between forest.
- The Pekel et al. (2016) dataset used here does not include some small water bodies, which can be misclassified as snow under the current methodology.
- Single-year SP values could capture half of the peak SWE variability over the Tuolumne domain; this skill is dependent on having sufficient cloud-free images that year between April and snow depletion. Multiple-year SP values were used for the rest of the study because they include more images and highlight snowcover features that persist between years. With the addition of other sensors (see bullet below), variability in snowcover indices between years may provide insights to changing controls on snowcover.
- Finally, we only used images from Landsat-8 and Sentinel-2A. The snowcover indices can be extended to years prior to 2013 by including historical Landsat images. Going forward, the addition of Sentinel-2B in March 2017 increases the number of cloud free images.

6. Summary

Snowcover indices using Landsat-8 and Sentinel-2A images were developed and used to map snow redistribution features. The calculations were implemented in the Google Earth Engine (Gorelick et al., 2017) for efficiency and to easily allow transferability to other mountainous regions. The snowcover absence and persistence indices are available globally and thus fill a critical gap in snow redistribution observations over the majority of mountains terrain.

Snowcover indices were evaluated against both station measurements and LiDAR-based spatial distributions of both snow depth and SWE. Over an intensely instrumented ridge in the Canadian Rockies (0.34 km^2), the remotely sensed indices captured the relative differences in snow presence and absence between wind-exposed and vegetation-sheltered weather station sites. Within the Tuolumne River Bain domain in central California (1100 km^2), the snow persistence index captured roughly half of the spatial variability ($R^2 = 0.49$ to 0.56 between years) of SWE, as derived from airborne LiDAR.

The relative controls of solar irradiance (ablation) and snow redistribution by wind and gravity on persistent snowcover features represent a significant outcome of this research. Over the Transect domain (21,118 km^2) in the Canadian Rockies there was no relationship ($R^2 = 0.09$) between shortwave irradiance and the snow persistence index. Over individual ridges (~800 m) where shortwave irradiance differences on each side of the ridge were the greatest, snow persistence appears to be strongly related to potential ablation energy ($R^2 = 0.76$) from shortwave irradiance. Yet the difference in energy for melt across the ridges was shown to be relatively small compared to the estimates of peak SWE, suggesting melt energy cannot alone be controlling snow persistence patterns. Snow redistribution from south to north facing slopes can contribute to snow persistence on some north facing slopes – such a situation has been documented in the mountains of the Yukon, Canada (Ménard et al., 2012; Pomeroy et al., 2003). Similarly, here persistent snowcover features (~100 m) were identified and classified as either snowdrifts or avalanche deposits, based on their relative topographic position of the SP maxima.

In summary, variability in both snow ablation and redistribution influenced the snow persistence index, but at different spatial scales. Thus, it is recommended that snowcover indices be used to evaluate snow redistribution models as long as variable insolation effects are also simulated. This has implications for snow hydrology modeling schemes for mountains and suggests that ideally, these models should deterministically estimate both the impacts of slope-based irradiance to capture snowmelt energy variability and redistribution of snow to capture meltwater availability, but with reference to the scale at which these processes are most evident. Finally, the snowcover indices have relevance to the fields of climatology, hydrochemistry, and snow ecology as snowcover persistence and location control atmospheric exchanges, nutrient fluxes, nival ecosystems and subsequent soil thaw and plant growth (Jones et al., 2001; Curtis et al., 2014, Wilson et al., 2016).

Acknowledgements

We would like to thank May Guan, Angus Duncan, Greg Galloway, Eric Courtin, and many students of the Centre for Hydrology for maintaining Fortress Mountain Snow Laboratory instruments and taking snow observations. NASA provided data from its Airborne Snow Observatory for Tuolumne River Basin. Funding was provided by NSERC Discovery Research Tools and Instrumentation grants, the NSERC Changing Cold Regions Network, the CFREF Global Water Futures Programme, the Canada Research Chair in Water Security, the Canada Research Chairs programme, the Canadian Foundation for Innovation, and Alberta Agriculture and Forestry. We are grateful to Fortress Mountain Ski Resort for assistance and access to the snow laboratory and the University of Calgary Biogeoscience Institute for

logistical support for the Coldwater Laboratory. GEE scripts to produce snowcover indices are provided at (https://code.earthengine.google.com/0fc31697a8cd8a961b7c4a1929c8c5a0). Code to calculate shortwave irradiance distribution available at (https://github.com/Chrismarsh/CHM). Fortress station data and analysis scripts will be made available upon request.

References

Aksamit, N.O., Pomeroy, J.W., 2016. Near-surface snow particle dynamics from particle tracking velocimetry and turbulence measurements during alpine blowing snow storms. Cryosphere 10, 3043–3062. http://dx.doi.org/10.5194/tc-10-3043-2016.

Benn, D.I., Evans, D.J.A., 1998. Glaciers & Glaciation, 2nd ed. Arnold, London. http://dx.doi.org/10.1017/CBO9781107415324.004.

Bernhardt, M., Liston, G.E., Strasser, U., Zängl, G., Schulz, K., 2010. High resolution modelling of snow transport in complex terrain using downscaled MM5 wind fields. Cryosphere 4, 99–113. http://dx.doi.org/10.5194/tc-4-99-2010.

Bintanja, R., Lilienthal, H., Tüg, H., 2001. Observations of snowdrift over Antarctic snow and blue-ice surfaces. Ann. Glaciol. http://dx.doi.org/10.3189/172756401781819076.

Brown, T., Pomeroy, J.W., 1989. A blowing snow detector. Cold Reg. Sci. Technol. 16, 167–174.

Clark, M.P., Hendrikx, J., Slater, A.G., Kavetski, D., Anderson, B., Cullen, N.J., Kerr, T., Örn Hreinsson, E., Woods, R.A., 2011. Representing spatial variability of snow water equivalent in hydrologic and land-surface models: a review. Water Resour. Res. 47, W07539.

Curtis, J.A., Flint, L.E., Flint, A.L., Lundquist, J.D., Hudgens, B., et al., 2014. Incorporating Cold-Air Pooling into Downscaled Climate Models Increases Potential Refugia for Snow-Dependent Species within the Sierra Nevada Ecoregion, CA. PLOS ONE 9 (9), e106984. http://dx.doi.org/10.1371/journal.pone.0106984.

Dadic, R., Mott, R., Lehning, M., Burlando, P., 2010. Wind influence on snow depth distribution and accumulation over glaciers. J. Geophys. Res. 115. http://dx.doi.org/10.1029/2009JF001261.

De Scally, F.A., 1992. Influence of avalanche snow transport on snowmelt runoff. J. Hydrol. 37, 73–97.

DeBeer, C.M., Pomeroy, J.W., 2010. Simulation of the snowmelt runoff contributing area in a small alpine basin. Hydrol. Earth Syst. Sci. 14, 1205–1219. http://dx.doi.org/10.5194/hess-14-1205-2010.

Deems, J.S., Fassnacht, S.R., Elder, K.J., 2006. Fractal distribution of snow depth from Lidar data. J. Hydrometeorol. 7, 285–297. http://dx.doi.org/10.1175/JHM487.1.

Déry, S.J., Salomonson, V.V., Stieglitz, M., Hall, D.K., Appel, I., 2005. An approach to using snow areal depletion curves inferred from MODIS and its application to land surface modelling in Alaska. Hydrol. Process. 19, 2755–2774. http://dx.doi.org/10.1002/hyp.5784.

Dozier, J., Frew, J., 1990. Rapid calculation of terrain parameters for radiation modeling from digital elevation data. IEEE Trans. Geosci. Remote Sens. 28, 963–969.

Fang, X., Pomeroy, J.W., 2009. Modelling blowing snow redistribution to prairie wetlands. Hydrol. Process. 23, 2557–2569. http://dx.doi.org/10.1002/hyp.

Farr, T., Rosen, P., Caro, E., Crippen, R., Duren, R., Hensley, S., Kobrick, M., Paller, M., Rodriguez, E., Roth, L., Seal, D., Shaffer, S., Shimada, J., Umland, J., Werner, M., Oskin, M., Burbank, D., Alsdorf, D., 2007. The shuttle radar topography mission. Rev. Geophys. 45, 1–33. http://dx.doi.org/10.1029/2005RG000183.1.INTRODUCTION.

Garnier, B.J., Ohmura, A., 1970. The evaluation of surface variations in solar radiation income. Sol. Energy 13, 21–34.

Gascoin, S., Lhermitte, S., Kinnard, C., Bortels, K., Liston, G.E., 2013. Wind effects on snow cover in Pascua-Lama, Dry Andes of Chile. Adv. Water Resour. 55, 25–39. http://dx.doi.org/10.1016/j.advwatres.2012.11.013.

Golding, D.L., 1978. Calculated snowpack evaporation during chinooks along the eastern slopes of the Rocky Mountains in Alberta. J. Appl. Meteorol. 1647–1651.

Gorelick, N., Hancher, M., Dixon, M., Ilyushchenko, S., Thau, D., Moore, R., 2017. Google earth engine: planetary-scale geospatial analysis for everyone. Remote Sens. Environ. http://dx.doi.org/10.1016/j.rse.2017.06.031.

Grünewald, T., Schirmer, M., Mott, R., Lehning, M., 2010. Spatial and temporal variability of snow depth and ablation rates in a small mountain catchment. Cryosphere 4, 215–225. http://dx.doi.org/10.5194/tc-4-215-2010.

Gubler, H., 1981. An electronic remote snow-drift gauge. J. Glaciol. 27, 164–174.

Hall, D., Riggs, G., Salomonson, V., 1995. Development of methods for mapping global snow cover using moderate resolution imaging spectroradiometer data. Remote Sens. Environ. http://dx.doi.org/10.1016/0034-4257(95)00137-P.

Hansen, M.C., Potapov, P.V., Moore, R., Hancher, M., Turubanova, S.A., Tyukavina, A., Thau, D., Stehman, S.V., Goetz, S.J., Loveland, T.R., Kommareddy, A., Egorov, A., Chini, L., Justice, C.O., Townshend, J.R.G., 2013. High-resolution global maps of 21st-century forest cover change. Science(80). http://dx.doi.org/10.1126/science.1244693.

Hopkinson, C., Chasmer, L., 2009. Testing LiDAR models of fractional cover across multiple forest ecozones. Remote Sens. Environ. 113, 275–288. http://dx.doi.org/10.1016/j.rse.2008.09.012.

Hough, P.V.C., 1962. Method and means for recognizing complex patterns. US Patent 3, 069,654. https://doi.org/10.1007/s10811-008-9353-1.

Housman, I., Tanpipat, V., Biswas, T., Clark, A., Stephen, P., Maus, P., Megown, 2015. Monitoring Forest Change in Southeast Asia: Case Studies for USAID Lowering Emissions in Asia's Forests. Salt Lake City.

Jones, H.G., Pomeroy, J.W., Walker, D.A., 2001. Snow Ecology. Cambridge University Press, Cambridge.

Lapo, K.E., Hinkelman, L.M., Landry, C.C., Massmann, A.K., Lundquist, J.D., 2015. A simple algorithm for identifying periods of snow accumulation on a radiometer. Water Resour. Res. http://dx.doi.org/10.1002/2015WR017590.

Li, D., Wrzesien, M.L., Durand, M., Adam, J., Lettenmaier, D.P., 2017. How much runoff originates as snow in the western United States, and how will that change in the future? Geophys. Res. Lett. 44, 6163–6172. http://dx.doi.org/10.1002/2017GL073551.

Lloyd, S.P., 1982. Least squares quantization in PCM. IEEE Trans. Inf. Theory. http://dx.doi.org/10.1109/TIT.1982.1056489.

Lundquist, J.D., Roche, J.W., Forrester, H., Moore, C., Keenan, E., Perry, G., Cristea, N., Henn, B., Lapo, K., McGurk, B., Cayan, D.R., Dettinger, M.D., 2016. Yosemite hydroclimate network: distributed stream and atmospheric data for the Tuolumne River watershed and surroundings. Water Resour. Res. 52, 7478–7489. http://dx.doi.org/10.1002/2016WR019261.

Macander, M.J., Swingley, C.S., Joly, K., Raynolds, M.K., 2015. Landsat-based snow persistence map for northwest Alaska. Remote Sens. Environ. 163, 23–31. http://dx.doi.org/10.1016/j.rse.2015.02.028.

MacDonald, M.K., Pomeroy, J.W., Pietroniro, A., 2009. Parameterizing redistribution and sublimation of blowing snow for hydrological models: tests in a mountainous subarctic catchment. In: Hydrological Processes, http://dx.doi.org/10.1002/hyp.7356.

MacDonald, M.K., Pomeroy, J.W., Pietroniro, A., 2010. On the importance of sublimation to an alpine snow mass balance in the Canadian Rocky Mountains. Hydrol. Earth Syst. Sci. 14, 1401–1415. http://dx.doi.org/10.5194/hess-14-1401-2010.

MacDonald, M.K., Pomeroy, J.W., Essery, R., 2018. Water and energy fluxes over northern prairies as affected by chinook winds and winter precipitation. Agric. For. Meteorol. 248, 372–385. http://dx.doi.org/10.1016/j.agrformet.2017.10.025.

Margulis, S.A., Cortés, G., Girotto, M., Huning, L.S., Li, D., Durand, M., 2016. Characterizing the extreme 2015 snowpack deficit in the sierra Nevada (USA) and the implications for drought recovery. Geophys. Res. Lett. 43, 6341–6349. http://dx.doi.org/10.1002/2016GL068520.

Meehl, G., Stocker, T., Collins, W., Friedlingstein, P., Gaye, A.T., Gregory, J.M., 2007. Global climate projections. In: Climate Change 2007: the Physical Science Basis. Contribution of Working Group I to the Fourth Assessment Report of the Intergovernmental Panel on Climate Change Cambridge University Press, United Kingdom and New York, NY, USA, pp. 1–8.

Ménard, C.B., Essery, R., Pomeroy, J., Marsh, P., Clark, D.B., 2012. A shrub bending model to calculate the albedo of shrub-tundra. Hydrol. Process. 28, 341–351. http://dx.doi.org/10.1002/hyp.9582A.

Musselman, K.N., Pomeroy, J.W., Essery, R.L.H., Leroux, N., 2015. Impact of windflow calculations on simulations of alpine snow accumulation, redistribution and ablation. Hydrol. Process. 29, 3983–3999. http://dx.doi.org/10.1002/hyp.10595.

Natural Resources Canada, 2007. Canadian Digital Elevation Data, Level 1 Product Specifications.

Otsu, N., 1979. A threshold selection method from gray-level histograms. IEEE Trans. Syst. Man Cybern. 9, 62–66. http://dx.doi.org/10.1109/TSMC.1979.4310076.

Painter, T.H., Berisford, D.F., Boardman, J.W., Bormann, K.J., Deems, J.S., Gehrke, F., Hedrick, A., Joyce, M., Laidlaw, R., Marks, D., Mattmann, C., McGurk, B., Ramirez, P., Richardson, M., Skiles, S.M.K., Seidel, F.C., Winstral, A., 2016. The airborne snow observatory: fusion of scanning lidar, imaging spectrometer, and physically-based modeling for mapping snow water equivalent and snow albedo. Remote Sens. Environ. 184, 139–152. http://dx.doi.org/10.1016/j.rse.2016.06.018.

Palm, S.P., Yang, Y., Spinhirne, J.D., Marshak, A., 2011. Satellite remote sensing of blowing snow properties over Antarctica. J. Geophys. Res. Atmos. 116, 1–16. http://dx.doi.org/10.1029/2011JD015828.

Pekel, J.-F., Cottam, A., Gorelick, N., Belward, A.S., 2016. High-resolution mapping of global surface water and its long-term changes. Nature 540, 418–422. http://dx.doi.org/10.1038/nature20584.

Pomeroy, J.W., Gray, D.M., 1995. Snowcover accumulation, relocation and management. Hydrol. Sci. J. http://dx.doi.org/10.1080/02626669509491396.

Pomeroy, J.W., Li, L., 2000. Prairie and arctic areal snow cover mass balance using a blowing snow model. J. Geophys. Res. 105, 26619. http://dx.doi.org/10.1029/2000JD900149.

Pomeroy, J.W., Gray, D.M., Shook, K.R., Toth, B., Essery, R.L.H., Pietroniro, A., Hedstrom, N., 1998. An evaluation of snow accumulation and ablation processes for land surface modelling. Hydrol. Process. 12, 2339–2367. http://dx.doi.org/10.1002/(SICI)1099-1085(199812)12:15<2339::AID-HYP800>3.0.CO;2-L.

Pomeroy, J.W., Toth, B., Granger, R.J., Hedstrom, N.R., Essery, R.L.H., Sciences, E., Kingdom, U., Canada, E., 2003. Variation in surface energetics during snowmelt in a subarctic mountain catchment. J. Hydrometeorol. 4, 702–719. http://dx.doi.org/10.1175/1525-7541(2003)004<0702:VISEDS>2.0.CO;2.

Pomeroy, J., Essery, R., Toth, B., 2004. Implications of spatial distributions of snow mass and melt rate for snow-cover depletion: observations in a subarctic mountain catchment. Ann. Glaciol. 38, 195–201. http://dx.doi.org/10.3189/172756404781815275.

Prokop, A., 2008. Assessing the applicability of terrestrial laser scanning for spatial snow depth measurements. Cold Reg. Sci. Technol. http://dx.doi.org/10.1016/j.coldregions.2008.07.002.

RGI Consortium, 2017. Randolph Glacier Inventory – a Dataset of Global Glacier Outlines: Version 6.0: Technical Report. http://dx.doi.org/10.7265/N5-RGI-60.

Scarchilli, C., Frezzotti, M., Grigioni, P., De Silvestri, L., Agnoletto, L., Dolci, S., 2010. Extraordinary blowing snow transport events in East Antarctica. Clim. Dyn. 34, 1195–1206. http://dx.doi.org/10.1007/s00382-009-0601-0.

Schirmer, M., Wirz, V., Clifton, A., Lehning, M., 2011. Persistence in intra-annual snow depth distribution: 1. Measurements and topographic control. Water Resour. Res. 47, 1–16. http://dx.doi.org/10.1029/2010WR009426.

Schmidt, R.A., Jairell, R.L., 1987. A System that Monitors Blowing Snow in Forest Canopies. Gen. Tech. Rep. - US Dep. Agric. For. Serv.

Schön, P., Prokop, A., Vionnet, V., Guyomarc'h, G., Naaim-Bouvet, F., Heiser, M., 2015. Improving a terrain-based parameter for the assessment of snow depths with TLS data in the col du lac blanc area. Cold Reg. Sci. Technol. http://dx.doi.org/10.1016/j.coldregions.2015.02.005.

Smith, D., McCarthy, D., Luckman, B., 1994. Snow-avalanche impact pools in the Canadian Rocky Mountains. Arct. Alp. Res. 26 (2), 116–127. http://dx.doi.org/10.2307/1551774.

Sturm, M., Holmgren, J., Liston, G.E., 1995. A seasonal snow cover classification system for local to global applications. J. Clim. http://dx.doi.org/10.1175/1520-0442(1995)008<;1261:ASSCCS>;2.0.CO;2.

Sturm, M., Goldstein, M.A., Parr, C., 2017. Water and life fromsnow: a trillion dollar science question. Water Resour. Res. 53, 3534–3544. http://dx.doi.org/10.1002/2017WR020840.

Vionnet, V., Guyomarc'h, G., Naaim Bouvet, F., Martin, E., Durand, Y., Bellot, H., Bel, C., Puglièse, P., 2013. Occurrence of blowing snow events at an alpine site over a 10-year period: observations and modelling. Adv. Water Resour. http://dx.doi.org/10.1016/j.advwatres.2012.05.004.

Vionnet, V., Martin, E., Masson, V., Lac, C., Bouvet, F.N., Guyomarc'h, G., 2017. High-resolution large eddy simulation of snow accumulation in alpine terrain. J. Geophys. Res. Atmos. http://dx.doi.org/10.1002/2017JD026947.

Whitfield, P.H., 2017. Clustering of seasonal events: a simulation study using circular methods. Commun. Stat. Simul. Comput. 1–23. http://dx.doi.org/10.1080/03610918.2017.1367805.

Wilson, A., Bacher, K., Breckheimer, I., Lundquist, J.D., Rochefort, R., Theobald, E., Whiteaker, L., HilleRisLambers, J., 2016. Monitoring Wildflower Phenology using Traditional Science, Citizen Science, and Crowd Sourcing. Park. Sci. 33, 17–26.

Zhang, T.Y., Suen, C.Y., 1988. A modified fast parallel algorithm for thinning digital patterns. Pattern Recogn. Lett. 7, 99–106. http://dx.doi.org/10.1016/0167-8655(88)90124-9.